



Universidad Nacional Autónoma de México

Instituto de Radioastronomía y Astrofísica

**Towards a definitive framework in the models
of dust emission in Active Galactic Nuclei**

Progress of the doctoral project

PRESENTS:

M.Sc. Omar Ulises Reyes Amador

ADVISORS:

PhD. Jacopo Fritz

PhD. Omaira González-Martín

November 2022

1 Introduction

1.1 The Unification Scheme

The “Unification Scheme” (or Unified Model) proposed by Antonucci (1993) is the most accepted model that is able to explain the diversity of Active Galactic Nuclei (AGN) and explain the different characteristics observed in type 1 as compared to type 2 objects. According to this scheme the center of all AGN hosts a supermassive black hole (SMBH) surrounded by an accretion disk that is heated up to $\sim 10^5$ K, and a region of clouds of gas moving at velocities of $\sim 10^4$ km s $^{-1}$, commonly called broad-line region (BLR). The last two components are the responsible for producing the strong ultraviolet (UV)/optical emission and the broad emission lines, respectively. At distances from the center where the temperature is lower than $\sim 10^3$ K, dust can coagulate (Maiolino et al., 2001) surviving to the intense radiation field. Dust is distributed in a geometrically and optically thick toroidal structure, known as “dusty torus”, which surrounds the AGN (see figure 1). Other important AGN components such as the hot corona, the narrow-line region (NLR), the relativistic jet and the ionization cone are illustrated in figure 1), but the study of the physical properties of these components are not aim of this work.

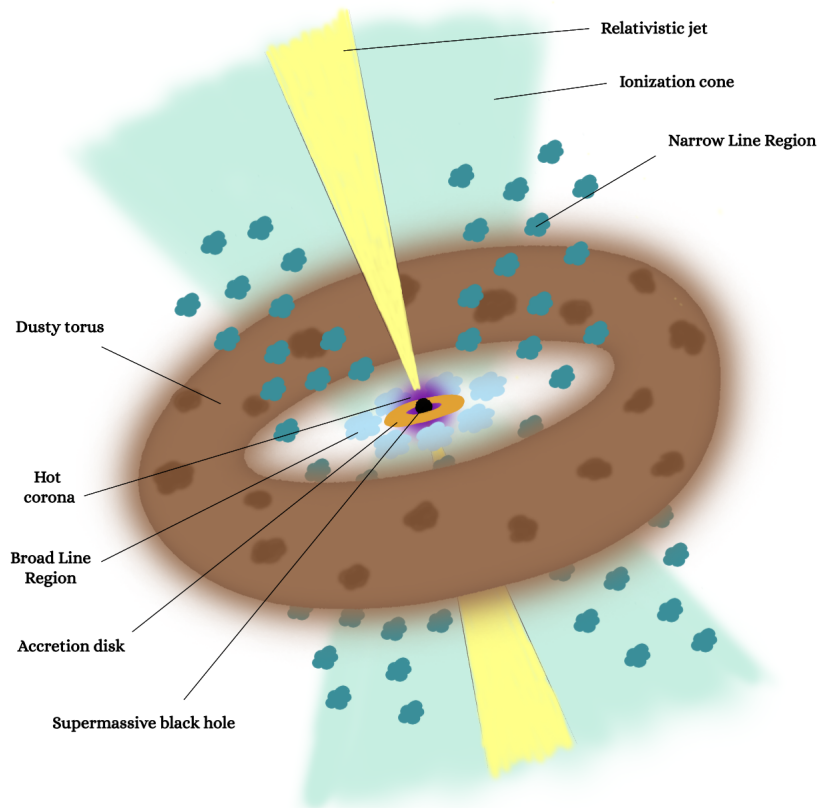


Figure 1: Artistic representation of the structure and components of an AGN according to the Unification Scheme (Reyes-Amador, in prep.). From the inside out, the supermassive black hole (in black) surrounded by the accretion disk (in orange) and its hot corona (in purple), and the region of ionized gas clouds (in light blue) which produce the broad emission lines. Further away is the region of ionized gas clouds (in dark cyan) which produce the narrow emission lines and the dusty torus (in brown). In the perpendicular direction is the relativistic jet (in yellow) and the ionization cone (in light blue-green).

1.2 The importance of the dusty torus

If the observer’s line-of-sight (LOS) crosses the dusty torus (edge-on view), the radiation coming from the accretion disk and the BLR is blocked. As a result, the object appears as a type 2 AGN only showing narrow emission lines in the spectrum -coming from clouds located much further away (the NLR)- and the strong UV/optical emission known as “Blue Bump” (shown in left panel of figure 2) is absent in the spectral energy distribution (SED). When the LOS does not cross the dusty torus, both the accretion disk and the BLR are exposed to the observer. Thus, broad emission lines and the blue bump can be observed and the object appears as a type-1 AGN. Therefore, this Unification Scheme suggests that the differences between type-1 and type-2 AGN are mostly due to an orientation effect. This picture was confirmed by observations of polarized broad emission lines in type 2 objects produced by scattering of electrons and dust (Antonucci and Miller, 1985; Moran et al., 2000; Nagao et al., 2004; Moran, 2007; Trump et al., 2011; Pan et al., 2019).

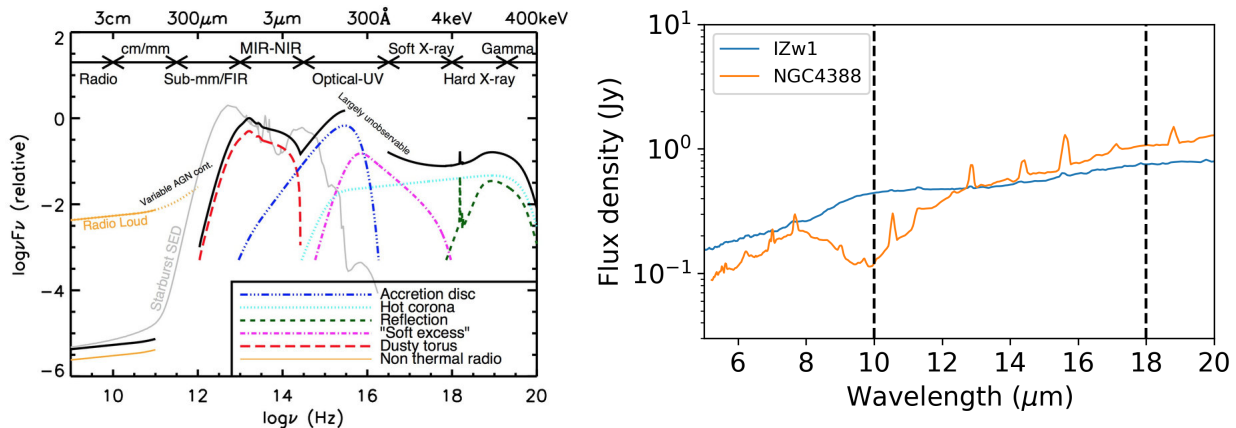


Figure 2: Left: Schematic representation of an AGN SED where the components emitted by the accretion disk (Blue Bump, in blue) and the dusty structure (Infrared Bump, in red) can be observed. The black line represents the total SED of a radio-quiet quasar and the colored lines represent its individual components. Figure taken from Baldini (2015). Right: 5-20 μm range of *emphSpitzer*/IRS spectra of a type-1 (IZw1, blue) and a type-2 (NGC 4388, orange) AGN. The black dashed vertical lines are at 10 and 18 μm . Note that the silicate feature at $\sim 10 \mu\text{m}$ is in emission (absorption) for the type 1 (type 2).

The dusty torus is expected to absorb the radiation coming from the accretion disk and re-emit it at infrared (IR) wavelengths. In addition to the observation of polarized broad emission lines in type 2 AGN, more evidence for the existence of this dusty structure comes from the observed strong infrared emission that ranges from ~ 1 to $\sim 50 \mu\text{m}$ called “Infrared Bump” in the spectral energy distribution (SED) of AGN (see left panel of figure 2). Furthermore, support of the AGN dust component is given by the observed emission features at ~ 10 and $\sim 18 \mu\text{m}$, which are produced by silicates as observed in the interstellar medium (ISM) (see section 2.1). In type-1 AGN, these features are expected to be detected in emission since the hot dust at the inner radius of the torus can be observed directly. Mid-IR (MIR) observations obtained with the *Spitzer* space telescope have confirmed the presence of such emission feature in AGN. On the other hand, due to obscuration by the cold dust located further out in the torus, the silicate features are observed in absorption in type 2 objects (Jaffe et al., 2004; Xu et al., 2020). Right panel of figure 2 shows the spectra of type-1 and type-2 AGNs from our sample with the $\sim 10 \mu\text{m}$ silicate feature in emission and absorption, respectively.

Additional evidence of the dusty torus comes from interferometric observations of the Seyfert 2 NGC 1068 (Wittkowski et al., 1998; Weigelt et al., 2004; Jaffe et al., 2004; Gravity Collaboration et al., 2020b) that resolved sub-pc and few pc structures. Tristram et al. (2007) reported evidence of a resolved dust structure in the Circinus galaxy using VLTI observations. Kishimoto et al. (2011) reported evidence of inner radial structures in type-1 AGN obtained with the Keck interferometer. Also, Gravity Collaboration et al. (2020a) have partially resolved the structure of hot dust that is heated by the central engine of a sample of type-1 AGN.

2 State of the art

In this section, we present how radiative transfer (RT) models of dust have been in charge of trying to explain physical properties of dust in AGN until then (Siebenmorgen et al., 2005; Hao et al., 2005; Sturm et al., 2005; Mason et al., 2009; Xie et al., 2017; González-Martín et al., 2019).

2.1 Silicates and graphite emission in AGN

The Near-IR (NIR) to MIR continuum emission in AGNs has been associated with a thermal dust emission in a range of temperatures from 1000 to 1800 K. In the infrared SEDs of a sample of Seyfert galaxies has been observed a NIR excess (Rieke, 1978) which for many AGNs has been modelled by Barvainis (1987) using graphite dust grains at their sublimation temperature of ~ 1800 K. The presence of hot dust very close to the central accretion disk in type-1 AGN has been confirmed by Minezaki et al. (2004) and Suganuma et al. (2006) using the reverberation mapping technique.

Of the variety of dust grains, silicates and graphite can survive in the AGN torus. Unlike silicate grains that have a sublimation temperature of ~ 1000 K, graphite grains can survive in the innermost regions of the torus due to their higher sublimation temperature. Hot dust was thought to be outside the BLR for NGC 4151 (Ferland and Mushotzky, 1982). In fact, more recently, it was found that pure graphite dust is located between the BLR and the dusty torus (Mor and Trakhtenbrot, 2011; Mor and Netzer, 2012) and it dominates the SED in the 2-5 μm region over the power-law emission from the accretion disk.

On the other hand, since late 1960s, the detection of silicates in the universe had been reported. First in the galactic ISM, for example: as emission in the Orion Nebula (Stein and Gillett, 1969) and later as absorption toward the Galactic center (Hackwell et al., 1970). Also, it is well known that spectral features observed at ~ 10 μm in Seyfert galaxies are produced by silicate grains (Rieke and Low, 1975; Kleinmann et al., 1976). Numerous infrared studies of many types of active galaxies typically invoke silicate grains (e.g., Hao et al. (2005, 2007); Siebenmorgen et al. (2005); Sturm et al. (2005); Mason et al. (2009); Xie et al. (2017)). The main evidence of silicate grains is the presence of two spectral features around 10 and 18 μm , in the MIR SED of AGNs. These features are attributed to the Si-O stretching and O-Si-O bending modes of amorphous silicates (Smith et al., 2010). Typically, the silicate features in galaxies are modelled using the optical and calorimetric properties of “astronomical silicates” calculated by Draine and Lee (1984); Laor and Draine (1993); Weingartner and Draine (2001); Draine (2003); Min et al. (2007); Draine and Li (2007). Works such as Siebenmorgen et al. (2005); Fritz et al. (2006); Nenkova et al. (2008b); González-Martín et al. (2019) have provided good fits to the MIR data of various galaxies which predict silicate in emission for type-1 AGN.

The MIR emission of some galaxies have shown these silicate features with some atypical characteristics: the peak of one or both features is red-shifted, their shapes are broader and the relative intensity of the feature at ~ 18 μm is greater than the one at ~ 10 μm (Smith et al., 2010; Sturm et al., 2005; Li et al., 2008). These “anomalous” silicate emission features have not been well predicted by any of the models mentioned above. This kind of “anomalous” silicate emission features have been modelled by Markwick-Kemper et al. (2007); Smith et al. (2010); Srinivasan et al. (2017) using alternative dust compositions whose optical properties have been experimentally determined in laboratory (Dorschner et al., 1995; Begemann et al., 1997; Jäger et al., 2003; Hofmeister et al., 2003). Markwick-Kemper et al. (2007) modelled the MIR spectrum of the BAL quasar PG 2112+059 using a power-law continuum and corundum, periclase, amorphous and crystalline silicates for the silicate features. Smith et al. (2010) considered two dust populations, warm and cold, in fitting the MIR emission of M 81. They modelled the dust using a porous composite mixture of amorphous silicate, amorphous carbon, and vacuum.

One of the aims of this work is to explore this kind of chemical compositions that are suggested to be formed in the existing conditions of AGN environments (Elvis et al., 2002; Srinivasan et al., 2017).

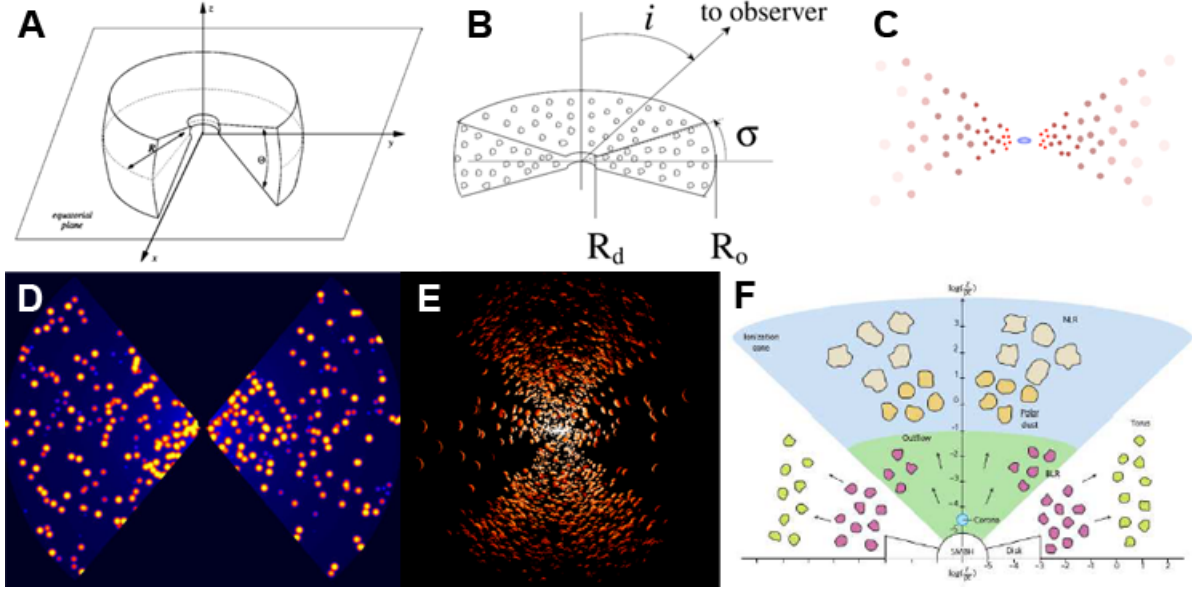


Figure 3: Edge-on views (except the A) of the dusty torus models proposed by different authors. (A) Fritz et al. (2006); (B) Nenkova et al. (2008b); (C) Hönic et al. (2006); (D) Stalevski et al. (2016); Hönic and Kishimoto (2017); (F) Ramos Almeida and Ricci (2017).

2.2 Modelling of the infrared dust emission and the problem

Since the 1990s, efforts in modelling the infrared SED of AGN produced by the dusty torus (hereinafter, dusty torus model) have been made using different methods and characteristics. It is well known that the primary source of an AGN is an accretion disk that emits an intense UV/optical continuum. This disk is usually modelled as a point-like source with isotropic emission (Schartmann et al., 2005; Fritz et al., 2006; Stalevski et al., 2012). Based on observations and theoretical considerations (e.g. Rowan-Robinson, 1995; Schartmann et al., 2005), the SED of the primary source has been approximated by a composition of power laws with different spectral indices in different spectral ranges (e.g. Rowan-Robinson, 1995; Hönic et al., 2006; Fritz et al., 2006; Nenkova et al., 2008a; Stalevski et al., 2012).

The first work attempting a RT modelling of the spatial dust distribution around the primary source was done by Pier and Krolik (1992). Pier and Krolik (1992) assumed a torus model with a cylindrical geometry and a homogeneous (smooth) dust distribution. Nowadays the geometry of the dusty torus is usually approximated with a flared disk (e.g. Fritz et al., 2006; Nenkova et al., 2008a,b; Stalevski et al., 2012, 2016). This is the simplest axisymmetric structure that can be defined in spherical coordinates and takes into account most of the ideas of the AGN unification scheme. It is defined by the inner and outer radius, R_{in} and R_{out} , respectively, the half opening angle Θ , the equatorial optical depth τ_ν and the parameters of the dust density distribution. To define the inner radius, authors commonly adopt the prescription given by Barvainis (1987) for a certain sublimation temperature (usually 1500 K for graphite).

Further investigations that have used such a smooth distribution for the dust in the torus were carried on by Granato and Danese (1994); Efstathiou and Rowan-Robinson (1995); van Bemmell and Dullemond (2003); Schartmann et al. (2005); Fritz et al. (2006). On the other hand, several authors have investigated a clumpy dust distribution (dust arranged in clouds) for the torus. This configuration is believed to be more physically motivated and, in some cases, is able to explain observational features in the torus SED. Results of RT calculations of such clumpy distribution have been performed by Nenkova et al. (2002, 2008a,b); Dullemond and van Bemmell (2005); Hönic et al. (2006, 2010, 2013); Hönic and Kishimoto (2010, 2017). Also, a combination of clumpy and smooth distributions for the dusty torus, called “two-phase medium”, has

been proposed (Stalevski et al., 2012, 2016; Siebenmorgen et al., 2015). Recently, an outflowing polar wind of dust and gas was proposed as a new component for tori models (Hönig et al., 2010; Hönig and Kishimoto, 2010, 2017) but with some ad hoc” assumptions (e.g. large grain size, no silicate grains) and some works have explored its role in the IR observations (Leftley et al., 2018; Williamson et al., 2019; Stalevski et al., 2019; Venanzi et al., 2020). Figure 3 show examples of these mentioned smooth, clumpy, two-phase and disk+wind models. Finally, in order to produce the inferred IR emission of the AGN, hydro-dynamical models, post-processed with RT codes to calculate dust emission, have been developed as well (Wada, 2012; Schartmann et al., 2014; Wada, 2015; Wada et al., 2016; Chan and Krolik, 2016; Williamson et al., 2019).

The dust mixture assumed on these models mostly consists of separate populations of graphite and silicate dust grains (or the standard composition of the interstellar medium). This assumption is based on some features in observed NIR and MID SEDs. (a) The emission at the shortest wavelengths implies dust temperatures above 1,000 K, something that only graphite grains can achieve (above these temperatures there are very efficient processes of destruction of the dust itself). (b) On the other hand, silicate grains have a lower sublimation temperature, around 800-1000 K, but their presence is clearly traced by the spectral features observed at ~ 10 and $\sim 18 \mu\text{m}$, typical of this dust species.

Another unknown is the relative distribution of grain sizes. This is commonly approximated as a power law with index $q = -3.5$, the classical MRN distribution (Mathis et al., 1977). However, evidence is emerging that, in AGN, the percentage of “large” size grains is higher than that normally found in the diffuse interstellar medium (e.g. Gonzalez-Martín et al. in prep.). The assumed range of grain sizes is different in almost all the models so far calculated in the literature. Some of them use different ranges for silicate and graphite (Fritz et al., 2006), others use the same (Stalevski et al., 2012, 2016), while others use only one average grain size (Hönig et al., 2006).

The scientific community is currently dealing with a rich set of dust emission models in AGN, each of them created with a different radiative transfer code and assuming fairly different ingredients: the SED of the accretion disk, chemical composition and grain sizes of dust, and the assumed dust density distribution. Yet, these models are basically only characterized by this latter aspect, biasedly considered as the one mainly defining their characteristics.

Furthermore, throughout the past years, the ability of a given model to reproduce either observed photometry + spectroscopy, or averaged SED properties (such as the intensity of the silicate features, the slope of the continuous emission), has been often used as a proof to claim that the characteristics of that particular model would correspond to the physical properties of the dusty torus, as opposed to other models with different characteristics (Nenkova et al., 2002; Nikutta et al., 2009). Such claims are -anyway- hard to sustain because of the many different working hypotheses and assumptions that each one of these models rely on. **Different geometries, dust properties, accretion disk SED and even RT codes (or approaches to the RT problem), are likely to play a role in determining the characteristics of the emitted spectrum: yet, such differences, are never considered as a possible source of bias in the results.**

This doctoral project **will produce a set of observationally-motivated model SEDs carefully choosing the accretion disk emission, geometry, composition and distribution of the AGN dust.** Furthermore, **we will explore all this diversity of models using the same radiative transfer code, allowing to study for the first time in an unbiased way the importance of each ingredient into the resulting SED library.**

3 Objectives

3.1 General objective

The general objective of this project is to establish a reference in the framework of radiative transfer models of dusty torus in AGN. This can be used for the analysis and interpretation of observed data, both present and future (e.g., VLTI, JWST, etc.). It will be achieved through the generation of a broader, more homogeneous

and complete set of theoretical/numerical models of dust emission in AGN in terms of exploring the space of physical parameters.

3.2 Specific objectives

1. **Characteristics of the dust grains:** Determine an appropriate chemical composition and grain sizes of the dust in AGN.
2. **Distribution of the dust:** Understand the role of the smooth, clumpy and two-phase distributions in the AGN dust models.
3. **The dust polar wind component and the Netzer disk:** Explore the role of polar dust winds and Netzer disks in the SED of AGN
4. **Observational testing of the models:** Confront our models with infrared observations to restrict the geometry, distribution, and composition of the AGN dust.

4 Observational data collection

To explore an appropriate chemical composition of dust in AGNs and because we are interested in the dust emission, mainly in the graphite continuous emission and the silicate features at ~ 10 and $18 \mu\text{m}$, a sample of nearby AGN with available infrared low resolution spectra is crucial. For that purpose, in this work, we used the sample studied by González-Martín et al, in prep. where a new synthetic SED library including the role of the maximum grain size into AGN dusty torus models is presented. This sample is composed by 68 AGN with available *Spitzer*/IRS spectra, good signal-to-noise ratio and fully dominated by the AGN dust at the MIR (5-35 μm) range. Among them, 43 are type-1 AGN and 25 are type 2 AGN. The sample include low- ($\log(L_X) \sim 41$, e.g. M 106), intermediate- ($\log(L_X) \sim 43.5$, e.g. IC 5063), and high-luminosity AGN ($\log(L_X) \sim 44.5$, e.g. PG 0804+761). Table 3 shows some observational data from the sample and further details on the sample selection can be found in the PhD research protocol.

Because of the model applied for the SED fitting assumes the emission region is optically thin at the wavelengths we are analyzing (see section 5.1 for details), in this work, we only used objects showing silicate emission features in their spectra. To discern those with silicate features in emission from those in absorption, the silicate strength (denoted as $S_{10\mu\text{m}}$) values calculated by (González-Martín et al., in prep.) were used. They obtained these values using the same prescription used by [Nenkova et al. \(2008b\)](#):

$$\text{Si}_\lambda = -\ln\left(\frac{F_\nu(\lambda)}{F_\nu(\text{continuum})}\right), \quad (1)$$

which uses the sign convention where absorption features have positive values and emission features have negatives. Table 3 shows the silicate strength values for each object. From the 68 objects of the complete sample, we obtained 49 objects with $S_{10\mu\text{m}}$ in emission, from which 41 are type 1 and eight are type 2. The remaining 19 objects have $S_{10\mu\text{m}}$ in absorption (two type 1 and 17 type 2). Figure 4 shows the spectra of objects with silicate features in emission and absorption (blue and gray, respectively). We can notice that, in most of the spectra, the peak of the $10 \mu\text{m}$ silicate emission feature is slightly shifted to longer wavelengths, while the peak of the $18 \mu\text{m}$ silicate emission feature is slightly shifted to shorter wavelengths. Also, note that data above $32 \mu\text{m}$ were not taken into account for the fitting because the signal-to-noise is significantly lower.

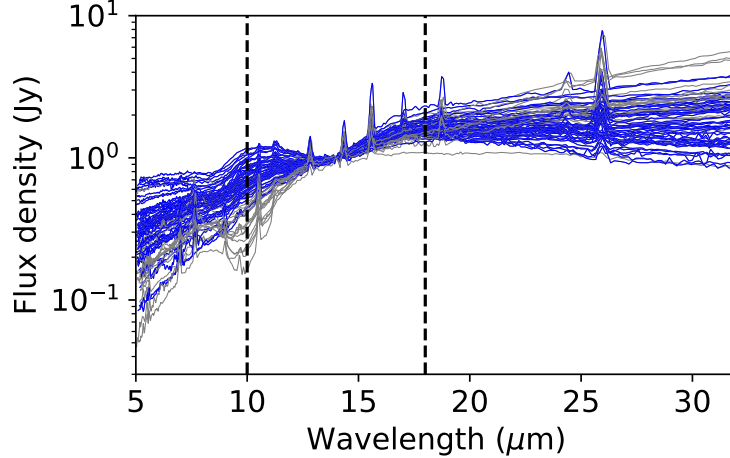


Figure 4: *Spitzer*/IRS spectra of the complete sample normalized to the flux at 14 μm . Objects with silicate features in emission (which are the focus of this work) and absorption are shown in blue and gray, respectively. The black dashed vertical lines are at 10 and 18 μm .

5 Methodology

In this section we describe the techniques implemented to achieve mainly the first specific objective of this research. Also, brief information about the RT code used to produce dusty torus models and the code used to explore the chemical composition and grain size of the dust is described.

5.1 Exploring the chemical composition and size of the dust grains.

The chemical composition and size of the dust grains of the dusty torus in a sub-sample of 49 AGN were explored through the SED fitting method. Our analysis on the chemical composition follows that reported by [Markwick-Kemper et al. \(2007\)](#) and [Srinivasan et al. \(2017\)](#). The former considers spherical grains with a fixed grain size and non-spherical grains with a fixed volume for corundum, periclase, olivine, Mg-rich olivine and forsterite. The latter uses just a continuous distribution of ellipsoids (CDE) with a fixed volume for the same dust species as [Markwick-Kemper et al. \(2007\)](#) and clinoenstatite. In contrast to them, in our analysis we have considered both spherical grains and CDE with different grain sizes and volumes, respectively. Also, those works use a sample of quasars while in this work, we use a sample of nearby Seyferts with some spectra with better data quality. They developed a mineralogy model to fit the MIR spectrum of each object, which is a linear combination of a number N of dust species superposed over a power-law continuum $F_c = A\lambda^\alpha$:

$$F_{\lambda,\text{mod}} = F_c \left(1 + \sum_{j=1}^N c_j Q_{\text{cs}}^{\lambda,j} \right), \quad (2)$$

where $Q_{\text{cs}}^{\lambda,j}$ and c_j are the continuum-subtracted extinction efficiency and the relative number of dust grains (or mass fraction) of the j^{th} dust species, respectively. This model is based on the following assumptions: (1) dust species producing the features and the continuum, have the same temperature (e.g. ([Siebenmorgen et al., 2005](#))), thus the mineralogy can be decoupled from the overall continuum in the form of a continuum-divided spectrum for which the temperature dependence is eliminated; (2) the emission region is optically thin at the wavelengths we are analyzing (5-32 μm), thus the continuum-divided spectrum yields the resulting opacity of the dust. We are allowed to use the latter assumption because only objects showing silicate emission

feature in their spectra are considered. Note that, because our analysis is focused on the AGN dust, while gas emission will not be taken into account in the subsequent radiative transfer models, we only considered the spectral characteristics produced by the dust emission. Like that, for the 49 spectra (from 5 to 32 μm), spectral lines produced by gas were masked in order to avoid their contribution to the spectral fitting of the model. We removed the data at the wavelengths where the spectral lines are observed in the spectra. These spectral lines can be easily identified in figure 4.

The procedure we use for the exploration of chemical composition of dust, is divided into three phases: (1) exploring the same continuum and dust species as [Srinivasan et al. \(2017\)](#) (2) exploring the most appropriate function for the continuum, and (3) exploring new and standard dust species and grain sizes.

Table 1: Chemical and physical information about dust species explored in this study.

Dust species label	Formula	Dust species name	Wavelength range (μm)	Grain density (g cm^{-3})	Grain sizes		Reference
(1)	(2)	(3)	(4)	(5)	(6)	(7)	(8)
Corundum	Al_2O_3	Porous Alumina	0.04 - 500	4.02	0.1	-	Begemann et al. (1997)
Periclase	MgO	Periclase	0.2 - 3333	3.56	0.1	-	Hofmeister et al. (2003)
Olivine	MgFeSiO_4	Olivine	0.2 - 500	3.79	0.1,1,2,3	0.1,1,2,3	Dorschner et al. (1995)
Mg_2SO_4	Mg_2SiO_4	Mg-rich Olivine	0.19 - 948	3.22	0.1	-	Jäger et al. (2003)
Forsterite	Mg_2SiO_4	Forsterite	0.2 - 852	3.2	0.1	-	Jaeger et al. (1998)
Enstatite	MgSiO_3	Clinoenstatite	0.04 - 98	3.28	0.1	-	Jaeger et al. (1998)
DLSil	-	Silicates	$0.04 - 10^5$	-	-	0.1-10*	Draine and Li (2007)
LDSil	-	Silicates	$10^{-3} - 10^3$	-	-	0.1-10*	Laor and Draine (1993)
MinSil	-	Silicates	$10^{-3} - 10^3$	-	-	0.1-8*	Min et al. (2007)

Notes: Columns 6 y 7 are the available grain sizes used in this study. (6) CDE: Characteristic radius at which the volume of a spherical grain is equal to the volume of a ellipsoidal grain. (7) Mie theory: radius of a spherical grain. MinSil are non-spherical grains.

*In this ranges, the used grain sizes are: for DLSil, 0.15, 1.19, 2.26, 3.46 and 4.27 μm ; for LDSil, 0.1, 1.0, 1.99, 3.16 and 3.98 μm ; for MinSil, 0.1, 1.0, 1.99, 3.16 and 3.98 μm .

5.1.1 Exploring the continuum and dust species from [Srinivasan et al. \(2017\)](#)

We adopted the same dust species and continuum prescription used by [Srinivasan et al. \(2017\)](#) for the model defined by eq. 2 to fit the spectra. In that work, they used the oxides porous alumina (corundum) and periclase, olivine and magnesium-rich (Mg-rich) olivine for amorphous silicates, and forsterite and clinoenstatite for crystalline silicates. Each of these is assumed to consist of a CDE of fixed volume, corresponding to a radius of 0.1 μm for spherical grains. Therefore, grains are ellipsoids of different grain sizes but the volume is fixed to the same value. Table 1 shows the name, label, formula, wavelength range of the available optical properties, grain density and grain size of each dust species.

For each dust species mentioned above, the continuum-subtracted extinction efficiency Q_{cs}^λ computed by [Srinivasan et al. \(2017\)](#) was used in this work. As for the observed spectra, this continuum subtraction was made in order to remove the continuum emission produced by the graphite thermal emission and leave only the silicate emission feature. The continuum emission is recovered for each dust species in the product of F_c and $Q_{\text{cs}}^{\lambda,j}$ from the eq. 2. The Q_{cs}^λ was computed using a robust polynomial fit anchored to the following wavelength ranges: 4-8 μm and 35-50 μm . This continuum-subtraction procedure was reproduced in our work for the dust species for which we computed the Q_{ext} values from the optical constants. This is explained in detail in section 5.1.3.

To compute the best fit to each spectrum using the model from eq. 2, [Srinivasan et al. \(2017\)](#) used the robust non-linear least squares curve fitting routing MPFIT ([Markwardt, 2009](#)) in IDL. In this work a Python version, called `AGNfitter` was developed. This code uses a given list of two column (wavelength in μm and Q_{cs}^λ) files corresponding to each dust species and, as an input, the spectrum of the object (a three column file:

wavelength in μm , flux and flux error). `AGNifitter` returns plots with the best fit (for the given spectrum) computed with a power-law continuum and the $Q_{\text{cs}}^{\lambda,j}$. In this case, the model has eight free parameters, two for the power-law continuum (A and α) and six for the dust species (one for each). Another output of this code is a file with values and uncertainties of the best-fit mass fractions for the dust species used in each model. As only one combination of six dust components (the six dust species) was considered for each object, only 49 fits were performed. Furthermore, I developed an algorithm called `dust_fitting` that executes `AGNifitter` to be applied to an input list of spectra and an input list of combinations of dust species. Apart from the aforementioned parameters, this code also calculates the χ^2_{ν} and AIC values from equations 6 and 7, respectively, for each combination and object; their values are saved in an output file. Moreover, for each combination and object it creates a file with the values of the spectral contribution of each dust species, calculated through their respective integral along the wavelength range of the spectrum.

5.1.2 Exploring the continuum shape

There are previous works where also MIR SED fitting in galaxies is carried out in order to analyze the silicate features (Spoon et al., 2007; Sirocky et al., 2008; Mendoza-Castrejón et al., 2015). As an example, Mendoza-Castrejón et al. (2015) used a cubic spline in logarithmic space over three fitting intervals to determine the continuum: the short-wavelength interval of 5-7 μm , the intermediate interval around 14 μm and the long-wavelength interval of 26.5-31.5 μm . In order to obtain the best fit for the continuum of MIR emission in AGN, in addition to a power-law function, we also used a cubic spline (or a third degree polynomial) to fit the continuum similarly to the works previously mentioned.

Therefore, two sub-versions of `AGNifitter` were made. One where F_c is modeled as a second degree polynomial (`AGNifitter_poly2`) and other as a third degree polynomial (`AGNifitter_poly3`). As in log-log space the power-law function becomes a straight line (first degree polynomial):

$$f(x) = p_1 x^{p_2} \iff \log[f(x)] = \log(p_1) + p_2 \log(x),$$

one term must be added to make it a 2nd deg. polynomial (hereinafter, `poly2`):

$$\log[f(x)] = \log(p_1) + p_2 \log(x) + p_3 (\log(x))^2,$$

and one more term to make it a 3rd deg. polynomial (hereinafter, `poly3`):

$$\log[f(x)] = \log(p_1) + p_2 \log(x) + p_3 (\log(x))^2 + p_4 (\log(x))^3.$$

These three algorithms consider the same six dust species described in section 5.1.1, differing only in the function used to fit the continuum. The three of them were applied to the 49 objects, and for each, the three models were compared using eq. 8. Finally, the distribution of ΔAIC for each continuum (power law, `poly2`, and `poly3`) was analyzed in order to obtain the function that best fits the continuum of the spectra.

5.1.3 Exploring new and standard dust species and grain sizes

It is well known that dust extinction is the property of dust that considers absorption and scattering of the radiation by the dust grains. These properties depend on the dust chemical composition, grain size and shape. In this work, as optical properties we refer to absorption, scattering or extinction efficiencies (or coefficients) of dust species. Optical properties of dust species mentioned in sections 5.1.1 and 5.1.2 were determined in laboratory (see table 1 for a summary of dust properties and works that calculated them). However, in section 2.1 we mention that silicate features are typically modelled using “astronomical silicates” whose optical properties have been inferred from astronomical observations of the ISM. All RT dusty torus models mentioned in section 2.2 use the standard ISM chemical composition. However, they use different optical

properties and grain sizes for the dust. Table 2 from [Martínez-Paredes et al. \(2020\)](#) shows these differences in the dust properties of the dusty torus models. In the assumed grain size range, most of them use a minimum grain size (a_{\min}) for graphite with size between 0.005 and 0.01 μm . Silicates a_{\min} usually have values between 0.005 and 0.05 μm . For both, the maximum grain size (a_{\max}) ranges between 0.25 and 1.0 μm . González-Martín et al., in prep. have explored the role of a_{\max} in this RT dusty torus models, finding that $\sim 90\%$ of the their sample require grains with a_{\max} different from 0.25 μm .

As we want to explore more possibilities about the chemical composition and size of the dust grains, both astronomical silicates and different grain sizes were taken into account. In this sense, searching in the documentation of the 3D radiative transfer code that is going to be used for the subsequent simulations (see section 5.2), files with optical properties of some silicates were found. These are absorption and scattering efficiencies (Q_{abs}^{λ} and Q_{sca}^{λ} , respectively) for silicates from [Laor and Draine \(1993\)](#), silicates from [Draine and Li \(2007\)](#) and silicates from [Min et al. \(2007\)](#) (hereinafter, LDSil, DLSil, MinSil, respectively). We calculated extinction efficiencies Q_{ext}^{λ} with $Q_{\text{ext}}^{\lambda} = Q_{\text{abs}}^{\lambda} + Q_{\text{sca}}^{\lambda}$. Silicates from [Laor and Draine \(1993\)](#) use the same optical constants as the original “astronomical silicates” calculated by [Draine and Lee \(1984\)](#) and an extension into the X-ray domain. [Draine and Li \(2007\)](#) uses the same properties as [Laor and Draine \(1993\)](#) for silicates (and graphites). The difference between them is that the former include polycyclic aromatic hydrocarbon (PAH) in their dust model. On the other hand, while previous references consider only amorphous silicates with an spherical shape, [Min et al. \(2007\)](#) consider both amorphous and crystalline silicates with a non-spherical shape. The optical properties for these dust species are available for more than 50 different grain sizes between 0.1 and 10 μm in almost all cases but, following the result obtained by González-Martín et al. in prep., we only used grain sizes of 0.1, ~ 1 , ~ 2 , ~ 3 and ~ 4 μm (see table 1 for the details).

In addition to the three different silicates mentioned above, the two oxides (porous alumina and periclase) and two amorphous silicates (olivine and Mg-rich olivine) from [Srinivasan et al. \(2017\)](#) were included in the fits. This gives us seven different dust species to deal with. In order to obtain optical properties for more grain sizes, both CDE and Mie, I developed the algorithm `dust_properties`. This calculates optical properties such as absorption, scattering and extinction coefficients, efficiencies and cross-sections for given complex refractive indices (also known as optical constants) n and k (not to be confused with the variables of the equations 4,6,7) and a given grain size using CDE or Mie theory. Only complex refractive indices for olivine and porous alumina were found in the literature ([Dorschner et al., 1995](#); [Begemann et al., 1997](#), respectively). For olivine, we calculated and used Q_{ext}^{λ} for both CDE and Mie grain sizes of 0.1, 1, 2 and 3 μm , while for porous alumina, periclase and Mg-rich olivine only a CDE grain size of 0.1 μm was used.

Then, we computed the Q_{cs}^{λ} for different sizes for olivine, DLSil, LDSil and MinSil. To do this, I developed the algorithm `continuum_subtractor`. It fits the continuum of the Q_{ext}^{λ} values for a dust species between two given anchor ranges, using a (n^{th}) degree polynomial, a (n^{th}) degree spline or a robust polynomial. Then, it computes Q_{cs}^{λ} by the subtraction of Q_{ext}^{λ} values minus the modeled continuum. To prove the algorithm works well, we tried to reproduce the Q_{cs}^{λ} for porous alumina using the same procedure followed by [Srinivasan et al. \(2017\)](#). This took a couple of weeks because I was obtaining different Q_{cs}^{λ} for porous alumina to those from [Srinivasan et al. \(2017\)](#) due to the fact that I was using Q_{ext}^{λ} calculated for Mie grain size of 0.1 μm and a 3rd degree polynomial to fit the continuum since I was developing the algorithms `continuum_subtractor` (it used to use splines or polynomials only) and `dust_properties` (it used to calculate Mie grain sizes only). Once I introduced the robust polynomial and CDE grain sizes to `continuum_subtractor` and `dust_properties`, respectively, I finally obtained the same Q_{cs}^{λ} values as [Srinivasan et al. \(2017\)](#) for porous alumina using a robust polynomial with anchor ranges 4-8 μm and 35-50 μm (see figure 5).

For DLSil, LDSil and MinSil with grain sizes of 0.1 μm (and 1 and 2 μm for LDSil), we used a robust polynomial to fit the continuum, while for grain sizes $> 0.1\mu\text{m}$ we used a 3rd deg. polynomial. Except for MinSil of 3 and 4 μm , and DLSil of 4 μm , for which I used a 2nd deg. polynomial. For olivine of CDE grain sizes of 0.1, 1, 2 and 3 μm , and Mie grain size of 0.1 μm , a robust polynomial was used, while for Mie grain

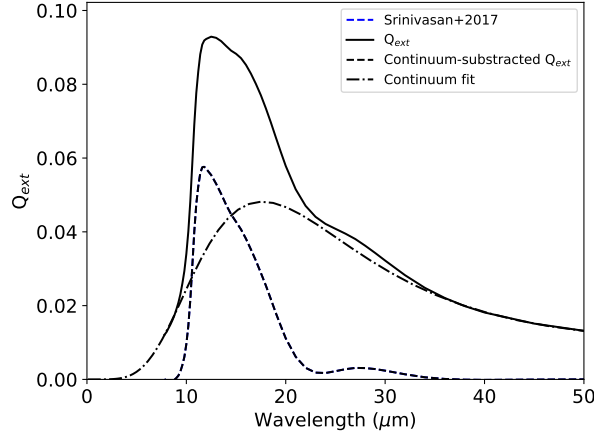


Figure 5: Extinction efficiency for porous alumina (corundum). The solid line is our calculated extinction efficiency Q_{ext} . The dash-dotted line is the robust polynomial fit representing the underlying continuum that we used to compute the continuum-subtracted Q_{ext} (black dashed line). Blue dashed line (covered by the black dashed line) is the continuum-subtracted Q_{ext} calculated by [Srinivasan et al. \(2017\)](#).

sizes of 1, 2 and 3 μm we used also a 3rd deg. polynomial.

The seven dust species with their respective grain sizes give us a total of 26 components (m) to test in the fits. However, since subtle differences in Q_{ext}^{λ} were observed between DLSil and LDSil, two sets of dust species were considered in order to avoid a degeneracy between these two silicates. The DL- and LD-sets, which consider DLSil and LDSil, respectively. Thus, each set has a total of $m = 21$ components. Also, in order to avoid a χ^2_{ν} degeneracy caused by the number of parameters k , different sub-sets of dust species combinations were tested: (1) a three-component set, (2) a four-component set, (3) a five-component set, and (4) a six-component set. Each set has all the possible combinations given by

$$C_{m,r} = \frac{m!}{(m-r)!r!}, \quad (3)$$

where r is the number of components of each set, i.e., for the three-component set, $r = 3$; for the four-component set, $r = 4$, etc. Considering the four sub-sets, these give us a number of 81,928 combinations for the DL-set. For the LD-set we use 67,172 combinations, which excludes the combinations already included in the DL-set. This number of fits was made considering both a power-law continuum and a poly3, such that the DL- and LD-sets were duplicated into those with power law (DL-PL-set and LD-PL-set) and those with poly3 (DL-poly3-set and LD-poly3-set). In total, 298,200 fits were performed for each of the 49 objects executing `dust_fitting`. As each fit takes ~ 1 minute to be done for the 49 objects, we spent ~ 14 days of computing time producing the fits in three computers, which simultaneously executed 5 fits each. Once finished, we used our developed algorithm `best_fits_combinations` to find the fits with AIC_{min} and those with $\Delta\text{AIC} \leq 10$ (see eq. 8 in the appendix A). Then, we compiled the statistical information in a table in order to facilitate the analysis.

5.2 RT simulations of the dusty torus models

Dust radiative transfer is a phenomenon that can be found in a lot of astrophysical scenarios such as star forming (SF) regions, AGNs and nebulae. This is a process that describes the interaction between radiation and matter at atomic scales. Thus, when matter and radiation coexists, it is necessary to solve the RT equation to calculate how they mutually interact and how the physical properties of each component can be affected by the other. One of the most popular and successful method to solve this problem, is through Monte Carlo (MC)

techniques. The first MC codes with RT applications were developed in the 1970s (Mattila, 1970; Roark et al., 1974; Witt, 1977). An important aspect of MC codes is that instead of looking for a numerical solution to the very complicated integro-differential radiative transfer equation, they simulate light-matter interactions by tracing the life and behavior of photon packages from random locations sampled from the source density distribution. Thanks to the development of technology and increase in the computational power, studies of three-dimensional (3D) RT have had an impressive advancement in the recent years. Many RT codes have been developed to calculate the physical properties of dust in astrophysical environments, most of them using the MC method (e.g. DustEM, Compiègne et al. (2011); SOC, Juvela (2019); POLARIS, Reissl et al. (2016)).

SKIRT¹ (Baes et al., 2011; Camps and Baes, 2015, 2020) is another 3D RT code that uses the MC method to emulate absorption, scattering and emission in dusty astrophysical systems such as galaxies, accretion disks, or SF regions. Its version 9 (the latest one) will be used in this work to produce the dusty torus models. Our choice is mainly dictated by four reasons: (1) Among the codes of this type, it is the one with the highest flexibility both in terms of available dust geometries and customizable options. (2) The code is on a continuous development track, and the developers are explicitly willing to take into account possible requests for modifications and additions to tackle unforeseen issues. (3) SKIRT is part of a project that includes many 3D RT codes, called 3D Benchmarks for the Transport of Radiation through a DUSTy Medium (TRUST²) which aims to define and provide a suite of benchmark problems that cover all the various numerical problems arising in dust RT. The benchmarks can be used to further develop and improve the existing codes as well as to test newly developed codes containing dust RT calculations. (4) This code has been already used by various authors to successfully produce dusty torus models and calculate their MIR emission (Stalevski et al., 2012, 2016, 2019; Victoria-Ceballos et al., 2022, González-Martín et al. in prep.).

Results obtained from section 5.1 will be taken to produce a grid of models with the best observationally motivated dust chemical composition and grain sizes, including all the mentioned characteristics and the polar wind component. Actually, we have already produced smooth, clumpy, two-phase, and disk+wind models with SKIRT as a test. This was done in order to familiarize with the technical procedure for creating the input file necessary to perform the simulations. Even more to test and learn how to use a different chemical composition than the default options offered by the code. To introduce a chemical composition specified by the user, it is necessary to provide an input file for each dust species with four parameters: (1) the extinction mass coefficient, (2) the scattering albedo, (3) the scattering asymmetry parameter, and (4) the wavelength. Thus, I developed the algorithm `dust_skirt_parameters_calculator` that calculates these four parameters through their respective optical constants found in the literature (see references in table 1).

6 Results

6.1 Silicate dust properties of the AGN torus

To present the results, hereinafter, we use a notation for the dust species. We use an abbreviation for the dust species name followed by a number that refers to the grain size. With PoAl, Per, Ol, MgOl, DL, LD, Min, we refer to porous alumina, periclase, olivine, Mg-rich olivine, DLsil, LDSil, MinSil, respectively. With the numbers 01, 1, 2, 3 and 4 we refer to grain sizes of 0.1, 2, 3, 4 μm . In the case of olivine, the abbreviation can be preceded by CDE or Mie, referring to the shape of the grain.

As mentioned in section 5, we explored a set of dust species and continuum emission that could be producing the observed characteristics in the *Spitzer*/IRS spectrum (5-32 μm) of our sample of 49 AGN with silicate emission features. Following the approach used by Markwick-Kemper et al. (2007); Srinivasan et al.

¹https://skirt.ugent.be/root/_landing.html

²<https://ipag.osug.fr/RT13/RTTRUST/obj.php>

(2017), we have found that a combination of the aforementioned dust species (see section 5.1.1) is able to successfully reproduce the great majority of the observed spectra in the sample: 46 out of the 49 selected objects have a fit model with $0 < \chi_\nu^2 < 2$ (objects with $\chi_\nu^2 > 2$ are: Mrk 1210, NGC 3783 and NGC 7213). However, taking into account the 49 objects, the mean $\chi_\nu^2 = 0.82$ and the median $\chi_\nu^2 = 0.59$. Moreover, all the objects have average residuals between -10 and 10% at wavelengths $> 8 \mu\text{m}$, which was considered as further evidence that a good fit was achieved. To summarize the result of the fitting, figure 6 shows the distributions of mass fraction for the six dust species. It is clear that, in terms of mass, porous alumina (corundum), periclase and olivine are the most important in the fits.

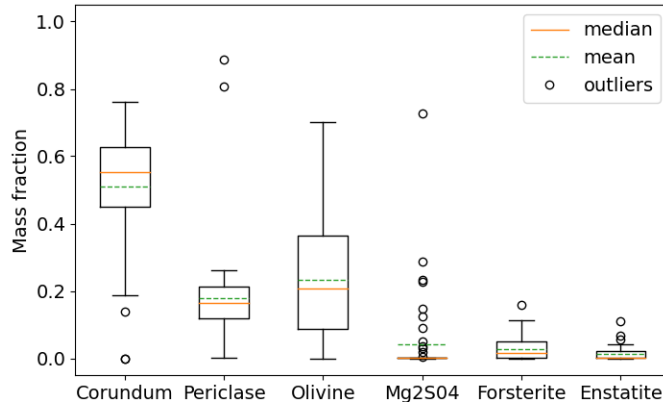


Figure 6: Distributions of mass fraction for each dust species used in the fits for the 49 AGN studied. The box extends from the lower to upper quartile values. Horizontal dashed and solid lines are the mean and the median, respectively. The whiskers extend from the box to show the range of the data. Flier points are those past the end of the whiskers.

Nevertheless, we noticed that, at wavelengths $< 8 \mu\text{m}$ for 17 out of 49 objects, the residuals were close or beyond the -10 and 10% limits. In order to address this issue and check the role of different functions for the continuum (see section 5.1.2), we used the poly2 and poly3 functions, obtaining that the optimization algorithm could not converge and hence no results could be obtained for the spectra of 24 objects. We suspected that one possible problem could have been of numerical nature, namely in the initial values of the parameters and in their boundaries used within the `scipy.optimize.curve_fit` function, which the `AGNifitter` and its sub-versions exploits in the best-fit model search. Hence, for these 24 objects only, we changed the values of the initial parameters and their bounds. In addition, we increased the maximum number of iterations.

With these changes, the algorithm was able to find optimal parameters to converge to an acceptable fit for the 24 objects. We obtained that, in general, the three functions achieve good fits with $0 < \chi_\nu^2 < 2$ for 46 objects of the sample (objects with $\chi_\nu^2 > 2$ are again Mrk 1210, NGC 3783 and NGC 7213). However, in terms of AIC values, we obtained important differences. Figure 7 shows that in almost all cases, in the comparison between the three different functions for the continuum, the median of $|\Delta\text{AIC}|$ is < 10 . However, in cases where power-law function is compared, $\sim 50\%$ of the objects have $|\Delta\text{AIC}| > 10$, which means that for $\sim 50\%$ of the objects, the poly2 and poly3 functions produce significantly better fits than a power law. In contrast, in the case where poly2 and poly3 are compared, only $\sim 20\%$ of the objects have $|\Delta\text{AIC}| > 10$.

The same analysis was repeated using optical properties of porous alumina, periclase, olivine and Mg-rich olivine, and also the optical properties of the standard astronomical silicates: DLSil, LDSil and MinSil, all of them with the grain sizes specified in section 5.1.3, and grouped them in the four sets of fits: (1) DL-PL-set, (2) LD-PL-set, (3) DL-poly3-set and (4) LD-poly3-set. We obtained that **DLSil and LDSil dust species give systematically similar results**. As we expected, in the 49 objects, fits using DLSil and those with LDSil do

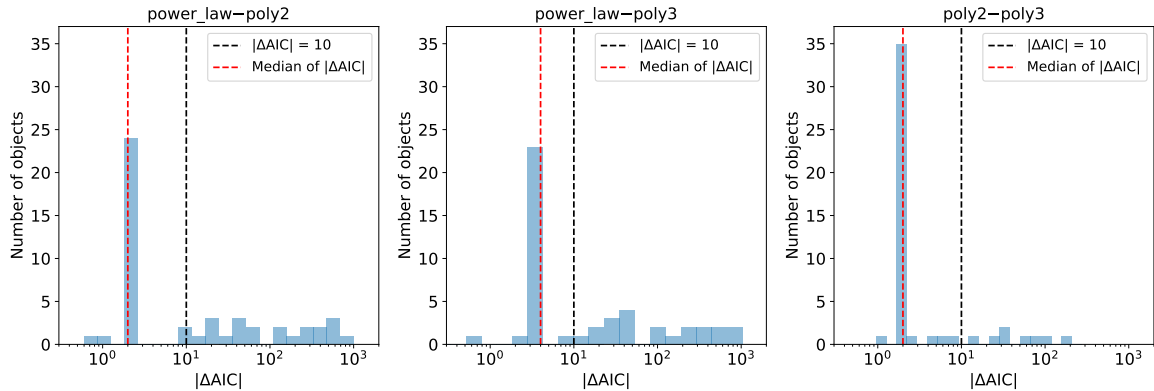


Figure 7: Distributions of $|\Delta\text{AIC}|$ values from the 49 fit models with different continuum. From left to right, $|\Delta\text{AIC}|$ values correspond to models using a power law minus models using a 2nd degree polynomial (poly2), power law minus 3rd degree polynomial (poly3), and poly2 minus poly3.

not show statistically significant differences between them since $\Delta\text{AIC} < 10$. As an example, figure 8 shows two fits for Ark 347 where we can see that there is no difference between both combinations of dust species, which are the same except for the last component. However, in all cases, the same combinations but with DLSil have slightly lower AIC values than those with LDSil. For this reason we proceeded to analyze the results of the set of fits in which DLSil was used instead of LDSil (DL-PL-set and DL-poly3-set). Moreover, we obtained that **PL and poly3 continua give systematically same results**. Comparing the pairs of fits with the same combination of dust species but with different function for the continuum, poly3 and PL, we obtained that $\Delta\text{AIC} < 10$. In other words, they do not have significant difference in all cases. As an example, figure 9 shows two fits for IZw1 with the same combination of dust species but different function for the continuum where we can see that there is no difference between poly3 and PL continua. Despite this, since we previously obtained that using poly3 to fit the continuum gives better fits than PL (see figure 7), we proceeded to analyze the results of the set of fits in which poly3 was used (DL-poly3-set). On the one hand, we found that the standard silicates, and CDE and Mie olivine with grain sizes between ~ 1 and $\sim 4 \mu\text{m}$ contribute to fit well the $10 \mu\text{m}$ silicate emission feature in the cases where it is shifted to longer wavelengths. On the other hand, $0.1 \mu\text{m}$ olivine grains, both CDE and Mie, help to fit well the the $18 \mu\text{m}$ silicate emission feature in the cases where it is shifted to shorter wavelengths.

The best-fit combination we selected for each object was the combination with AIC_{min} and the minimum number of components (or dust species). The best fits obtained for the 49 AGN are combinations mostly composed by four dust species (see top-left plot of the figure 10). However, each object has good-fit combinations with both a higher and lower number of components. These good-fit combinations have $|\Delta\text{AIC}| < 10$, meaning that they are equally good as its respective best fit. Using these results, we compiled the good-fit combinations for all objects and grouped them according to the number of components: three, four, five and six. Then, we selected and analyzed the 10 most frequent of each group finding that, in the four groups, the most common dust species in almost all the combinations are $0.1 \mu\text{m}$ porous alumina (PoAl01), $0.1 \mu\text{m}$ periclase (Per01), and both Mie and CDE olivine (MieOl and CDEOl) with different grain sizes. The bottom plot of figure 10 shows, as an example, the 10 most frequent good-fit combinations with four components, where we can see that $2 \mu\text{m}$ DLSil (DL2) and $0.1 \mu\text{m}$ Mg₂SO₄ (MgOl01) are present only in two good-fit combinations with a frequency of five and seven, respectively.

Taking into account only the best-fit combinations of the 49 AGN, we obtained that, from the 21 possible dust species to fit the spectrum (see section 5.1.3), 15 were used (see the top-right plot of figure 10). It is important to note that PoAl01 and Per01 were needed to obtain the best fits of almost all the objects. PoAl01

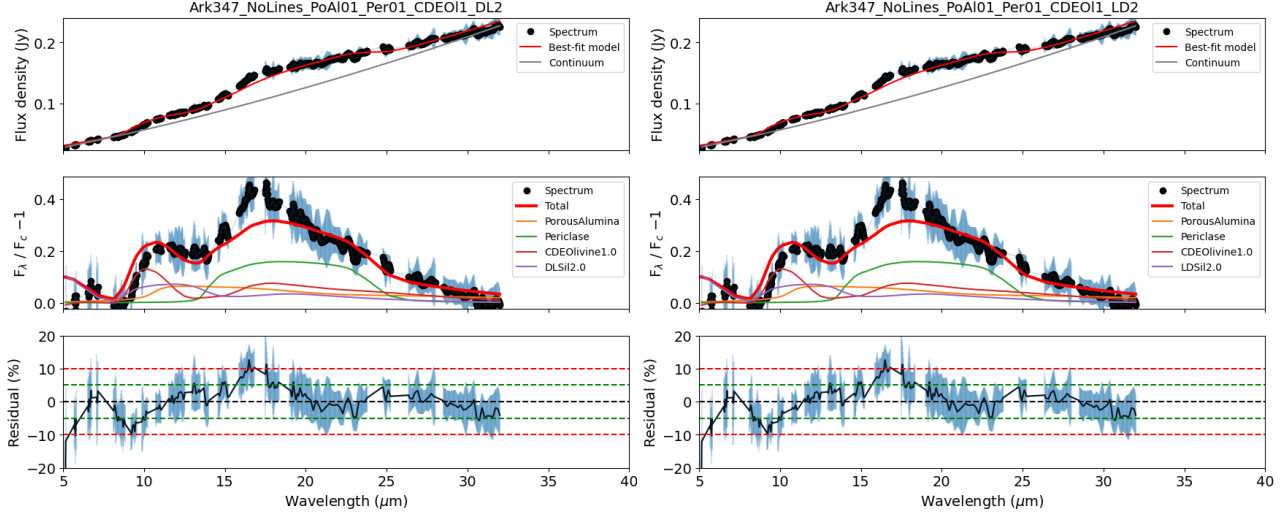


Figure 8: Fits of the MIR spectrum of Ark 347 with a combination composed by PoAl01, Per01, CDEO11 in both and DL2 (in left), and LD2 (in right). Any difference can not be seen between them. Upper panel shows the data (black points), their error bars (in blue), the best fit (red solid line) and the continuum (gray solid line) used in that best fit . Mid panel shows the data (black points), their errors (in blue), the fitted dust species (in colors) and the best fit (red thick solid line). Lower panel shows the residual normalized by the best fit in percentage (black solid line) and thresholds at 5% and 10% (green and red dashed lines, respectively).

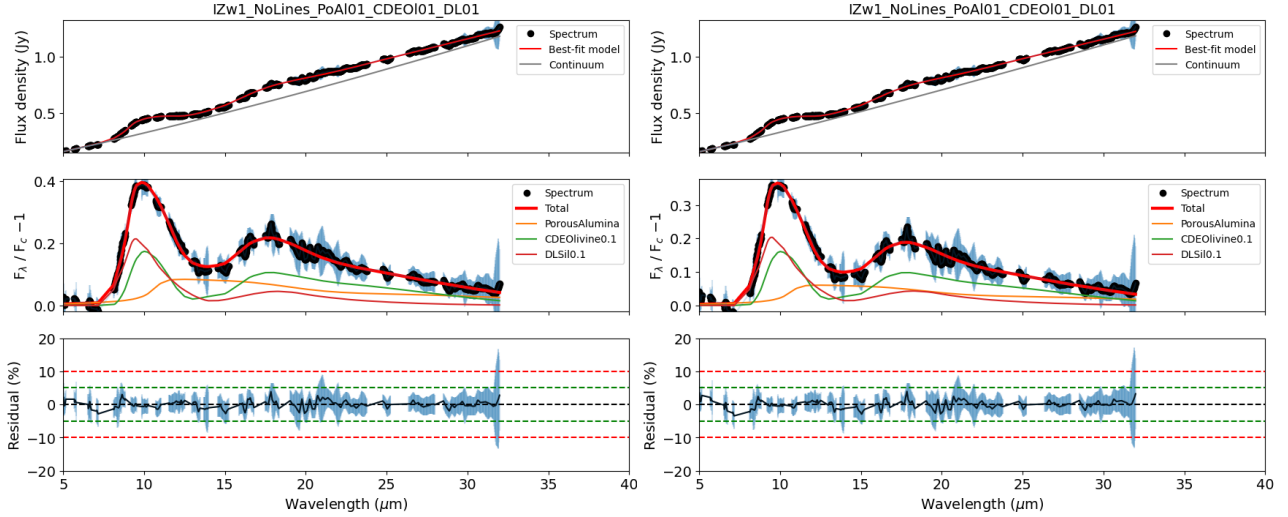


Figure 9: Fits of the MIR spectrum of IZw1 with a combination composed by PoAl01, CDEO11 and DL01. A poly3 (left) and a PL (right) were used for the continuum. Any difference can not be seen between them. The rest of the description is same as figure 8.

was not necessary only in one case (MCG -06-30-015) and Per01 in two cases (IZw1 and M 106). MieO11 and MieO13 are the dust species most frequent in the best fits after the two mentioned above.

We obtained the spectral contributions, which we show in figure 11, of each of the 15 dust species used in the best fits. We can see that PoAl01 and Per01 have the most important contribution with a median $> 30\%$ in all cases. Nevertheless, it should be noted that MieO12, CDEO11 and CDEO11 have important contribution ($\gtrsim 30\%$) as well in a few objects (see outliers in fig. 11). Taking into account the spectral contribution, the statistical frequency of each dust species, and the fact that more than 50% of the best fits are combinations of four dust species, we decided that the dust species that are most likely to represent the chemical composition of our sample of AGN with silicate emission features are PoAl01, Per01, MieO11

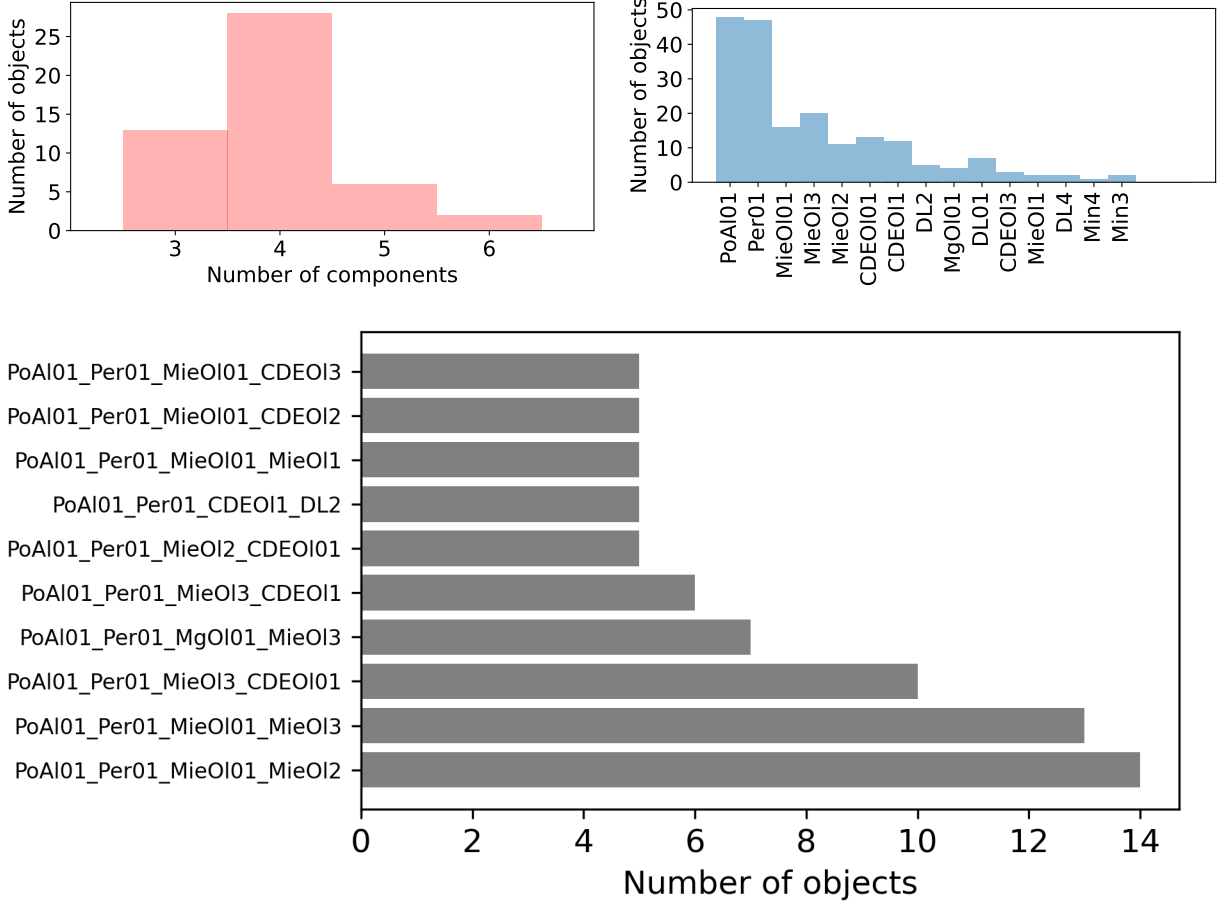


Figure 10: Top-left: Statistical frequency of the number of components (or dust species) used in the best fits of the 49 AGN. Top-right: Statistical frequency of the 15 dust species used in the best fits of the 49 AGN. Bottom: Statistical frequency of the 10 most repeated good-fit combinations with four components among the 49 AGN.

and MieOl3. **Another reason why we selected only these four dust species, is because one of the aims of this work is to produce dusty torus models through radiative transfer simulations using SKIRT, which allows us to introduce a mix of dust composed by a limited number of dust populations. The higher the number of dust populations, the longer the computation time, since it increases linearly with the number of grain size bins.**

We analyzed how the spectra of our sample are fitted with this particular combination composed by PoAlO1, PerO1, MieOlO1 and MieOl3, obtaining that the fits are globally good since the median of $\chi^2_\nu = 0.65$. and for almost all objects, the residuals are, in average, between -10 and 10% . Only in five objects (Mrk 1210, NGC 7213, PG 0804+761, PG 1211+143 and PG 1351+640) its respective fit gives $\chi^2_\nu > 2$. It is worth to mention that, although the fit of Mrk 1210 does not show an optimal χ^2_ν value, its average residuals are within 10% , while the fits of the remaining four objects are not able to reproduce well the $10 \mu\text{m}$ silicate feature. Inspecting the fits of this four objects, we obtained that MieOl2, CDEOl1, CDEOl3, DL01, DL2, Min3 are necessary to obtain their corresponding best-fits.

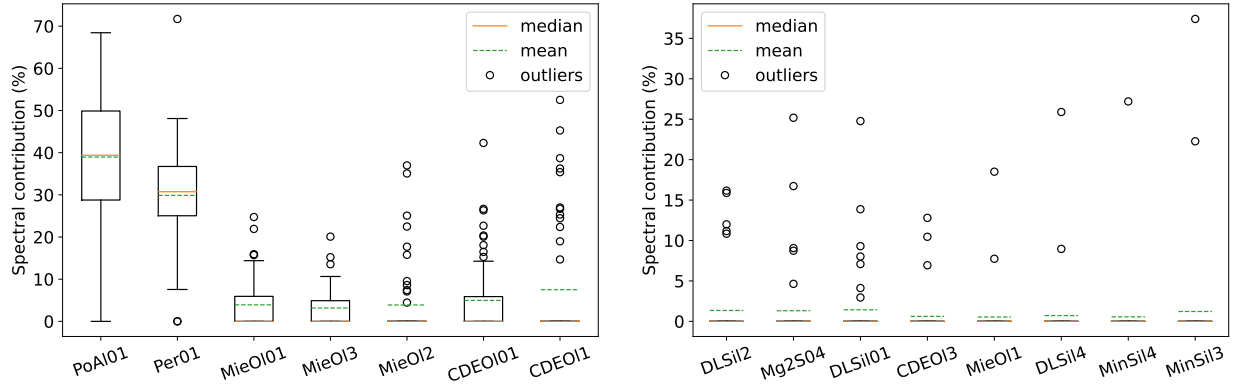


Figure 11: Distributions of spectral contribution in the best fits of the 15 dust species from the right panel in figure 10. Left panel shows the seven dust species found in the best fits of more than 10 objects, while the right panel shows those found in less than 10 objects. The rest of the description is same as figure 6.

6.2 Radiative transfer simulations

In this section we present preliminary results of RT simulations that we have made in order to familiarize with the parameters that version 9 of SKIRT needs to simulate dusty torus models with the specific characteristics of the dust density distributions that we want to study: smooth, clumpy, two-phase and disk+wind.

We have created simulations of each dusty torus model with different dust density distribution using the same values for their parameters in common. Table 2 shows the parameters of the dust system and the spatial grid used in SKIRT to simulate the different models. For the primary source, we used an isotropic point source with a luminosity of $10^{11} L_{\odot}$ and an SED composed by power laws. As an example, top panel of figure 12 shows cuts of the dust density along the xy and xz planes, corresponding to face-on and edge-on views, respectively and their SEDs obtained for a model with smooth dust density distribution.

Table 2: Testing models made with SKIRT.

Model	Dust system parameters										Spatial grid parameters					
	i	Θ	p	q	R_{in}	R_{out}	$\tau_{9.7}$	N_0	Clumpiness	Dust mix	No. phot. pack.	Grid resol. (pc/pix)	Log. wave. range (μm)	No. points		
(1)	(deg)	(deg)	(2)	(3)	(4)	(5)	(6)	(7)	(8)	(9)	(10)	(11)	(12)	(13)	(14)	(15)
Smooth	0/90	50	1	2	0.25	2.5	2					DL	10^6	0.025	0.001-1000	150
Clumpy	0/90	50	1	2	0.25	2.5	2	1000	0.9999			DL	10^6	0.025	0.001-1000	150
Two-phase	0/90	50	1	2	0.25	2.5	2	1000	0.25			DL	10^6	0.025	0.001-1000	150

Notes: Column 1: type of model according to its dust density distribution. Columns 2: viewing angle toward the torus. Column 3: opening angle. Column 4 and 5: indices of the radial and polar density distribution of the dust. Column 6 and 7: inner and outer radius. Column 8: equatorial optical depth at $9.7 \mu m$. Column 9: number of clumps. Column 10: fraction of total dust mass that is in the clumps. Column 11: optical properties of the dust mix. Column 12: number of photon packets. Column 13: resolution of the spatial grid. Column 14: range of the logarithmic wavelength grid. Column 15: number of points of the logarithmic wavelength grid.

Also we have created a simulation for a smooth dust density distribution using the chemical composition we obtained from the mineralogy model and dust species we use to fit the MIR spectra of our sample. For this simulation, we used the same parameter values as in the smooth model in table 2, except for the R_{in} and dust mix. For the former, we used an inner (or sublimation) radius of 0.79 pc, given by the sublimation temperature of silicates, $T = 1000$ K. For the latter, we used $0.1 \mu m$ porous alumina, $0.1 \mu m$ periclase, and Mie olivine of 0.1 and $3 \mu m$ introducing the parameters needed by SKIRT, which were calculated using `dust_skirt_parameters_calculator` and the optical constants of those dust species. We obtained a

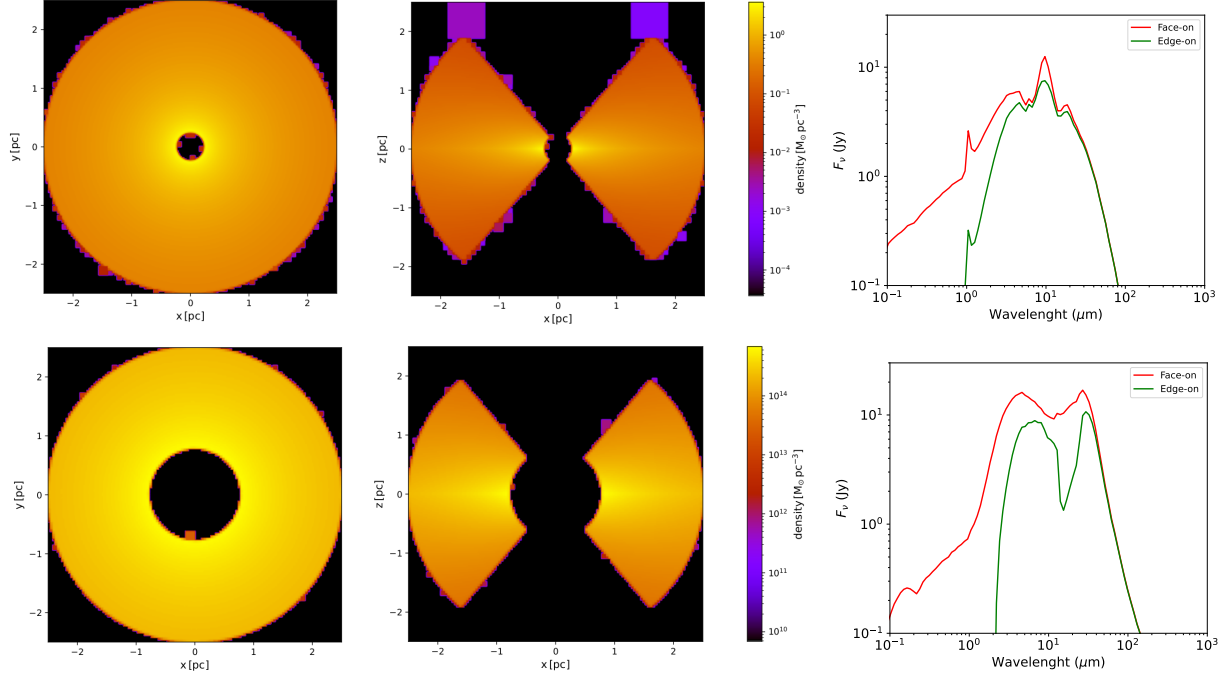


Figure 12: Both panels show the results of a simulation of a dusty torus with a smooth dust density distribution. Differences are that in the top panel we used a $R_{\text{in}} = 0.25$ pc and the dust mix of [Draine and Li \(2007\)](#), while in the bottom panel we used $R_{\text{in}} = 0.79$ pc and a dust mix composed by $0.1 \mu\text{m}$ porous alumina, $0.1 \mu\text{m}$ periclase, and Mie olivine of 0.1 and $3 \mu\text{m}$. Left and center panels show cuts of the dust density along the xy and xz planes, corresponding to face-on and edge-on views, respectively. The right panel shows their synthetic SEDs in face-on (red line) and edge-on (green) views.

synthetic data cube with the total surface brightness for each pixel and the total SEDs. Both output files are in face-on and edge-on views. Bottom panel of figure 12 shows cuts of the dust density along the xy and xz planes, corresponding to face-on and edge-on views, respectively and their SEDs obtained for this smooth model with the dust species we selected to represent the chemical composition of our sample of AGN with silicate emission features. This is a preliminary result that still needs to be analyzed.

7 Conclusions

We have implemented the SED fitting technique using *Spitzer/IRS* ($5\text{-}32 \mu\text{m}$) spectra of 49 AGN and a mineralogy model that is described by a linear combination of a number of dust species superposed over a continuum. We have explored three different functions meant to represent the continuum emission and a set of dust species for the silicate features consisted of oxides, amorphous silicates, and crystalline silicates, also including the standard astronomical silicates that have been used for decades in the literature. We used different grain sizes for dust species for which optical properties are available. This is the first time that all these dust species have been taken into account to model the MIR emission of AGN dust through the SED fitting technique. Also, this is the first time that the dust chemical composition of the torus is studied with the final goal of using an observationally motivated dust mixture in the construction of RT torus models, instead of assuming one.

We have concluded that the function used to model the continuum, among power law, poly2 and poly3, does not have an important role in obtaining a good fit, since the χ^2_{ν} and AIC values obtained in the best fits using these functions were similar. There is a large number of dust mixtures composed by dust species with different grain sizes and shapes (spheres and ellipsoids) that can be used to obtain a good fit of the MIR spectra

of the 49 AGN with silicate emission features studied in this work. However, as we need to select the most appropriate chemical composition that will be used in subsequent RT simulations instead of the commonly assumed standard astronomical silicates, we decided to choose a dust mix of porous alumina, periclase, both with grain sizes composed by continuous distribution ellipsoids with a characteristic grain size of $0.1 \mu\text{m}$, and olivine with spherical grain sizes of 0.1 and $3 \mu\text{m}$. This because is the chemical composition that, in general, best reproduces the observed characteristics of the silicate features in the MIR spectra our studied sample, concluding that large and small olivine grains produce the red-shifted $10 \mu\text{m}$ and blue-shifted $18 \mu\text{m}$ silicate emission features, respectively.

8 Future work

During these three semesters, we have mainly focused on the first objective of this PhD thesis, which is about the exploration of an appropriate chemical composition and grain size of the dust in the AGN dusty torus, in order to find the characteristics that best explain the observations of a sample of AGN with silicate emission features and, subsequently, introduce them into RT models of the dusty torus. Also, we have made progress in the production of the four prototype RT dusty torus models: smooth, clumpy, two-phase and disk+wind, and we have started to use the chemical composition we have found to produce simulations from a smoothly distributed dusty torus. We encountered difficulties that delayed some planned activities on the schedule. For example, we spent much more time than planned to explore the chemical composition and size of dust grains due to issues related with investigating their optical properties, computing the continuum-subtraction of Q_{ext} values, and producing and analyzing the 298,200 fits performed. These activities were planned to be finished in the second semester, but they extended to the third one. This is a slightly delay of the writing of the first paper about the chemical composition of AGN dust as planned in the schedule of the doctoral project. However, we have started to write a draft of the paper which we are planning to finish and submit during next semester. There are activities that still need to be done, while there are some that will no longer be done and have been removed from the schedule. Among those that will be carried out we have:

1. **The grid of models:** In the doctoral project, we presented the calculations of the computing time to produce the grid of models we need to simulate with SKIRT. This computing time has been calculated again, but this time, considering two more computers (four in total) simultaneously, and we obtained that the computing time required for the simulations will be $\lesssim 9$ months.
2. **Comparison with observational data:** This is the final part of this doctoral work. A comparison between the simulated dusty torus models and the data from the section 4 is crucial to analyze the goodness of the models. To do that, we will exploit techniques similar to those implemented by [Feltre et al. \(2012\)](#); [González-Martín et al. \(2019\)](#); [Martínez-Paredes et al. \(2020\)](#) which focus on the characteristics in both the observed and synthetic spectra from 5 to $32 \mu\text{m}$: (a) the infrared spectral slopes (b) the silicate feature strengths, and (c) the width of the IR bump.

- (a) **Infrared spectral slopes:** using the same definition as [González-Martín et al. \(2019\)](#), three slopes of the form

$$\alpha = -\frac{\log(F_\nu(\lambda_2)/F_\nu(\lambda_1))}{\log(\lambda_2/\lambda_1)},$$

with $\lambda_2 > \lambda_1$, will be computed. Note that, under this definition, negative (positive) values mean that the flux increases (decreases). This three slopes are α_{NIR} , α_{MIR} , α_{FIR} evaluated at $[\lambda_1, \lambda_2]$ equal to $[5.5, 7.5]$, $[7.4, 14]$, and $[25, 30] \mu\text{m}$, respectively.

- (b) **Silicate feature strengths:** This parameter will be calculated for both 10 and $18 \mu\text{m}$ silicate features using the equation 1.

- (c) **Width of the IR bump:** This has been used by [Granato and Danese \(1994\)](#); [Feltre et al. \(2012\)](#) as the \log_{10} of the frequency range in which the spectrum is more than 1/3 of its peak value (expressed in F_ν). This same definition will be used in this work.

To summarize the work have done (with a ✓) and that it is still pending, we present here an updated schedule of this project:

✓**1. First semester:** (a) I read the state of the art about AGN dusty tori models (smooth, clumpy, two-phase and disk-wind). (b) I familiarized with the concepts and the parameters of each model. (c) I made an algorithm that can create a file with a SED for an AGN composed by a combination of power laws and a Black Body. (d) I produced prototype dusty torus models in order to familiarize with the version 9 of SKIRT and its capabilities. (e) We wrote the doctoral project and its presentation. (f) I participated in the *IX Reunión de Estudiantes de Astronomía (IX-REA)* as an expositor where I presented a part of my master thesis.

✓**2. Second semester:** (a) We explored and identified the appropriate chemical composition and optical properties of the dust mix for AGN (b) I produced dusty torus models with SKIRT to explore the parameters of dust. (d) I attended (virtually) to the workshop Large-Volume Spectroscopic Analyses of AGN and Star Forming Galaxies in the Era of JWST.

✓**3. Third semester:** (a) I started to write a draft of the first paper about the chemical composition of AGN dust. (c) We produced a few smooth, clumpy, two-phase and disk+wind dusty torus models with the same global parameters for the primary source, the dust system, and the dust grid. (d) I will participate in the SKIRT days workshop in Ghent, Belgium and in the TORUS 2022 workshop on Leiden, Netherlands, where I will present the current results. (e) I will do a one-week research stay at UGent with prof. Marteen Baes, who is one of the main developers of the SKIRT code.

4. Fourth semester: (a) I will finish to write the first paper and I will send it. (b) We will produce the first part of smooth, clumpy and two-phase torus models. (c) We will compare our models with the observed sample. (d) I will start to write the second paper about the models with different dust distributions.

5. Fifth semester: (a) I will reply to the referee's comments of the first paper. (b) I will finish to write the second paper and I will send it. (c) I will run the first part of dusty torus models with the polar wind component. (d) We will explore the importance of the Netzer disk in our models with the polar wind component. (e) We will compare our first part of models with polar wind with the comparison sample.

6. Sixth semester: (a) I will reply to the referee's comments of the second paper. (b) I will run the last part of dusty torus models with the polar wind component. (c) We will compare our last part of models with polar wind with the comparison sample. (d) I will participate in a congress, workshop or similar. (e) I will write the third paper about the dusty torus models with polar wind component.

7. Seventh semester: (a) I will reply to the referee's comments of the third paper. (b) We will write the PhD thesis and it will be sent to the synod committee.

8. Eighth semester: (a) We will make the corresponding corrections to the thesis according to the indications of the synod committee. (b) We will develop a website to make all the models publicly available. (c) Finally, we will create slides to present the finished project on the graduation exam.

9 Bibliography

Akaike98, ISBN 978-1-4612-1694-0. •Antonucci+85, ApJ, 297, 621. •Antonucci+93, ARA&A, 31, 473. •Baes+11, ApJS, 196, 22. •Baldini+15, PhD thesis. •Barvainis87, ApJ, 320, 537. •Burnham&Anderson+04, doi: 10.1007/978-0-387-22456-5 5. •Begemann+97, ApJ, 476(1), 199. •Camps&Baes15, Astronomy and Computing, 9, 20. •Camps&Baes20, Astronomy and Computing, 31, 100. •Chan&Krolik16, ApJ, 825, 67. •Compiègne+11, A&A, 525, A103. •Dorschner+95, A&A, 300, 503. •Draine03, ApJ, 598(2), 1026. •Draine&Lee84, ApJ, 285, 89. •Draine&Li07, ApJ, 657(2), 810. •Dullemond&vanBemmel05, A&A, 436, 47. •Efstathiou&Rowan-Robinson95, MNRAS, 273, 649. •Elvis+02, ApJL, 567(2), L107–L110. •Esparza-Arredondo+21, A&A, 651, A91. •Feltre+12, MNRAS, 426, 120. •Ferland&Mushotzky82,

ApJ , 262, 564. •Fritz+06, MNRAS, 366, 767. •González-Martín+19, ApJ, 884, 11. •Granato & Danese94, MNRAS, 268, 235. •Dexter+20, A&A, 635, A92. •Pfuhl+20, A&A, 634, A1. •Hackwell+70, Nature , 227(5260), 822. •Hao+05, ApJL, 625, L75. •Hao+07, ApJL, 655(2), L77-. •Hofmeister+03, MNRAS , 345(1), 16 •Hönig+06, A&A, 452, 459. •Hönig&Kishimoto10, A&A, 523, A27. •Hönig+10, A&A, 515, A23. •Hönig+13, ApJ, 771(2), 87. •Hönig&Kishimoto17, ApJl, 838, L20. •Jaffe+04, Nature, 429,47. •Jaeger+98, A&A, 339, 904. •Jäger+03, A&A, 408, 193. •Juvela19, A&A, 622, A79. •Kishimoto+11, A&A, 527, A121. •Kleinmann+76, ApJ , 208, 42. •Laor&Draine+93, ApJ , 402, 441. •Leftley+18, ApJ, 862, 17. •Li+08, MNRAS, 391(1), L49. •Maiolino+01, A&A, 365, 37. •Markwick-Kemper+07, ApJL, 668(2), L107. •Martínez-Paredes+20, ApJ, 890, 152. •Martínez-Paredes+21, ApJ, 922(2), 157. •Mason+09, ApJL, 693, L136. •Mathis+77, ApJ, 217, 425. •Mattila+70, A&A, 9, 53. •Mendoza-Castrejón+15, MNRAS, 447(3), 2437. •Min+07, A&A, 462(2), 667. •Minezaki+04, ApJL, 600(1), L35. •Mor&Netzer12, MNRAS, 420(1), 526. •Mor&Benny11, ApJL, 737(2), L36. •Moran07, AGN conference, 373, 425. •Moran+00, ApJL, 540, L73. •Nagao+04, AJ, 128, 109. •Nenkova+02, ApJL, 570, L9. •Nenkova+08a, ApJ, 685, 147. •Nenkova+08b, ApJ, 685, 160. •Netzer87, MNRAS, 225, 55. •Nikutta+09, ApJ, 707(2), 1550. •Pan+19, ApJ, 870, 75. •Pier&Krolik92, ApJ, 401, 99. •Ramos Almeida+17, Nature Astronomy, 1, 679. •Reissl+16, A&A, 593, A87. •Rieke78, ApJ, 226, 550. •Rieke&Low+75, ApJL, 199, L13. •Roark+74, ApJ, 190, 67. •Rowa-Robinson95, MNRAS 272, 737. •Schartmann+05, A&A, 437, 861. •Schartmann+14, MNRAS, 445(4), 3878. •Siebenmorgen+05, A&A, 436, L5. •Siebenmorgen+15, A&A, 583, A120. •Sirocky08, ApJ, 678(2), 729. •Smith+10, ApJ, 716(1), 490. •Spoon+07, ApJL, 654(1), L49. •Srinivasan+17, PSS, 149, 56. •Stalevski+12, MNRAS, 420, 2756. •Stalevski+16, MNRAS, 458, 2288. •Stalevski+19, MNRAS, 484, 3334. •Stein&Gillett69, ApJL, 155, L197. •Sturm+05, ApJL, 629, L21. •Tristram+07, A&A, 474, 837. •Trump+11, ApJ, 732, 23. •Urry&Padovani+95 PASP, 107, 803. •Venzani+20, ApJ, 900, 174. •vanBemmel&Dullemond03, A&A, 404, 1. •Wada+12, ApJ, 758, 66. •Wada+15, ApJ, 812, 82. •Wada+16, ApJL, 828, L19. •Weigelt+04, A&A, 329, L45. •Williamson+09, ApJ, 876, 137. •Wittkowski+98, A&A, 329, L45. •Xie+17, ApJS, 228, 6. •Xu+20, RAA, 20, 147.

A Statistical hypothesis test

The Akaike information criterion (AIC, [Akaike, 1998](#)) was the statistical hypothesis test used in this study to measure the goodness of the fits. It estimates the quality of each model, relative to each of other models. The AIC has been implemented by [Esparza-Arredondo et al. \(2021\)](#); [Martínez-Paredes et al. \(2021\)](#), [González-Martín et al. in prep.](#)) to obtain the best fit. The AIC value of the model is defined by

$$\text{AIC} = 2k - 2 \ln(P), \quad (4)$$

where k is the number of free parameters while P is the value of the likelihood function for each model. In this study, the term of the likelihood was defined as following:

$$-2 \ln(P) \equiv \chi^2 = \sum_i \left(\frac{\text{data}_i - \text{model}_i}{\text{error}_i} \right)^2, \quad (5)$$

where error_i is the error associated to the i^{th} datum. Under this definition, the χ^2 of the best fit should approach to the degree of freedom (ν). Thus, letting be n the number of data, the reduced χ^2 (χ^2_ν) given by

$$\chi^2_\nu = \frac{\chi^2}{\nu} = \frac{\chi^2}{n - k}, \quad (6)$$

should be close to the unity. In this sense, equation 4 becomes

$$\text{AIC} = 2k + \chi^2. \quad (7)$$

In this work, delta AIC values (ΔAIC) were calculated to compare the models (or fits). The ΔAIC is the relative difference between the best model and each other model in the set. The formula is

$$\Delta\text{AIC} = \text{AIC}_i - \text{AIC}_{\min}, \quad (8)$$

where AIC_i is the value for the model i and AIC_{\min} is the value for the best model. [Burnham and Anderson \(2004\)](#) give the following rule of thumb for interpreting ΔAIC values: Models having (1) $\Delta\text{AIC} \leq 2$ have substantial support

(evidence), those in which $4 \leq \Delta\text{AIC} \leq 7$ have considerably less support, and models having $\Delta\text{AIC} > 10$ have essentially no support. In other words, if two models have $\Delta\text{AIC} \leq 10$, it means that they do not have a significant difference between them. On the other hand, if $\Delta\text{AIC} > 10$, it means there is significant difference. This last interpretation was used in this work to obtain the best model in the set of models described in our analysis.

B Sample data

Object name (1)	z (2)	Class (3)	$\log(L_X)$ (4)	$S_{10\mu m}$ (5)	Object name (6)	z (7)	Class (8)	$\log(L_X)$ (9)	$S_{10\mu m}$ (10)
Mrk 348	0.005	S2	43.86	0.220±0.008	I Zw 1	0.059	S1	43.85	-0.291±0.008
FAIRALL9	0.047	S1	44.09	-0.184±0.004	NGC 526A	0.019	S1	43.78	-0.136±0.004
NGC 788	0.014	S2	43.51	0.151±0.004	Mrk 1018	0.042	S1	42.82	-0.260±0.002
Mrk 590	0.021	S1	43.23	-0.200±0.004	NGC 1052	0.005	S1	42.24	-0.265±0.002
NGC 1275	0.016	S2	43.76	-0.393±0.008	ESO 548-G081	0.014	S1	43.29	-0.271±0.003
3C 120	0.033	S1	44.38	-0.305±0.004	MCG -01-13-025	0.016	S1	43.29	-0.575±0.001
CGCG420-015	0.029	S2	43.74	-0.138±0.005	2MASXJ05054575-2351139	0.035	S2	44.22	0.197±0.004
Ark120	0.032	S1	43.78	-0.266±0.006	PICTORA	0.035	S1	44.03	-0.502±0.002
2MASXJ05580206-3820043	0.034	S1	43.86	0.289±0.025	Mrk 3	0.014	S2	43.79	0.182±0.012
ESO 426-G002	0.022	S2	43.44	0.212±0.003	Mrk 78	0.037	S2	43.47	0.508±0.004
Mrk 1210	0.013	S1	43.37	-0.191±0.010	PG 0804+761	0.100	S1	44.46	-0.433±0.002
MCG +04-22-042	0.032	S1	43.73	-0.207±0.005	Mrk 110	0.033	S1	44.25	-0.243±0.002
Mrk 705	0.029	S1	43.41	-0.112±0.004	MCG -05-23-016	0.008	S2	43.53	0.298±0.024
NGC 3081	0.006	S2	43.07	0.157±0.007	ESO 374-G044	0.028	S2	43.64	-0.100±0.002
Mrk 417	0.033	S2	43.91	-0.107±0.004	2MASSXJ10594361+6504063	0.084	S2	43.48	0.811±0.003
ESO 439-G009	0.025	S2	43.27	0.426±0.003	NGC 3783	0.011	S1	43.56	-0.258±0.010
UGC6728	0.007	S1	42.40	-0.223±0.002	2MASXJ11454045-1827149	0.033	S1	44.08	-0.223±0.003
Ark347	0.022	S2	43.52	-0.095±0.027	NGC 4151	0.002	S1	43.17	-0.092±0.156
PG 1211+143	0.090	S1	43.70	-0.315±0.003	M 106	0.002	S1	41.06	-0.394±0.003
NGC 4388	0.005	S2	43.64	0.816±0.017	NGC 4507	0.012	S2	43.76	-0.193±0.015
NGC 4939	0.009	S2	42.81	-0.243±0.001	IISZ010	0.034	S1	43.52	-0.177±0.002
MCG -03-34-064	0.020	S1	43.28	0.301±0.015	MCG -06-30-015	0.008	S1	42.82	-0.112±0.009
IC 4329A	0.016	S1	43.77	-0.116±0.048	UM614	0.033	S1	41.74	-0.261±0.001
Mrk 279	0.030	S1	43.87	-0.108±0.006	PG 1351+640	0.088	S1	43.10	-0.854±0.002
NGC 5548	0.025	S1	43.76	-0.212±0.005	ESO 511-G030	0.015	S1	43.65	-0.365±0.002
PG 1448+273	0.065	S1	43.30	-0.140±0.002	IC 4518W	0.016	S2	43.19	1.370±0.013
Mrk 841	0.036	S1	44.01	-0.101±0.005	Mrk 1392	0.036	S1	43.74	-0.198±0.003
Mrk 1393	0.054	S1	43.80	-0.118±0.001	Mrk 290	0.030	S1	43.68	-0.225±0.002
ESO 138-G001	0.009	S2	42.55	-0.147±0.161	ESO 103-G35	0.013	S2	43.63	0.816±0.016
Fairall51	0.011	S1	43.22	-0.277±0.007	ESO 141-G055	0.037	S1	44.25	-0.344±0.003
NGC 6814	0.003	S1	42.59	-0.203±0.008	MCG +07-41-03	0.056	S2	44.57	0.680±0.005
IC 5063	0.009	S2	43.29	0.279±0.026	I Zw 136	0.078	S1	43.50	-0.068±0.004
NGC 7213	0.005	S1	42.46	-0.659±0.003	NGC 7314	0.004	S2	42.47	0.497±0.009
PG 2304+042	0.042	S1	43.40	-0.569±0.001	PKS 2356-61	0.096	S2	43.77	0.573±0.001

Table 3: Observational detail of the sample of AGN with *Spitzer*.